The Importance of Kinematic Configurations for Motion Control of Driving Simulators

Kolff, Maurice; Venrooij, Joost; Schwienbacher, Markus; Pool, Daan M.; Mulder, Max

DOI
10.1109/ITSC57777.2023.10422127

Publication date
2023

Document Version
Final published version

Published in
2023 IEEE 26th International Conference on Intelligent Transportation Systems, ITSC 2023

2023 IEEE 26th International Conference on
Intelligent Transportation Systems (ITSC)
24-28 September 2023. Bilbao, Bizkaia, Spain

The Importance of Kinematic Configurations for Motion Control of Driving Simulators

Maurice Kolff[1,2], Joost Venrooij[1], Markus Schwienbacher[1], Daan M. Pool[2], and Max Mulder[2]

***Abstract*— This paper describes how the kinematic configuration of a driving simulator's motion system affects the rendered inertial motion. The specific force and rotational rate equations between the point where the motion is applied (Motion Reference Point (MRP)), and the point in which the driver perceives the motion (Cueing Reference Point (CRP)), are derived for three kinematic configurations: (i) a hexapod, (ii) a hexapod with an xy-drive and a yaw-drive below, and (iii) the same system as (ii), but with the yaw-drive on top. The rotational rate equations show that having a yaw-drive on top greatly complicates the motion control. Furthermore, simulation results show that, regardless of the yaw-drive location, the difference between MRP and CRP becomes noticeable for large yaw-drive excitations. For such driving simulators, the positional offset between MRP and CRP can therefore not be ignored, complicating the motion control.**

I. Introduction

Driving simulators are important tools for automotive research as they provide a safe, cost-efficient, and controlled-environment alternative to real vehicle testing. Typical research examples are human-machine interaction [1], human-in-the-loop testing of vehicle safety systems [2], and human factors research on automated driving and traffic safety [3]. When employed with a motion system, its goal is often to mimic the inertial motion of the real vehicle as closely as possible to make the simulation more realistic. This conversion is performed by the Motion Cueing Algorithm (MCA) [4], which converts the simulated vehicle motion (typically, specific forces and rotational rates) to motion that retains the physical limits of the simulator. Poor motion reproduction can lead to decreased realism [5], simulator sickness [6], and unwanted adaptation of control behaviour [7], all negatively affecting the testing of vehicular technologies.

Many motion systems consist of a six Degree of Freedom (DoF) hexapod [8], also known as *Stewart* [9] or *Stewart-Gough* [10] platform. To improve the potential motion reproduction, a novel trend in state-of-the-art driving simulator technology is to extend the workspace of the six DoF hexapod using additional motion subsystems. This is commonly done using linear xy-drives (e.g., FKFS's simulator [11]), rotational yaw-drives (e.g., BMW's Sirius Vector [12]), or a combination of both (e.g., Toyota's Driving Simulator [13], Renault's ROADS [14], and BMW's Sapphire Space [12]). Although the additional workspace can improve the motion reproduction, the complexity of the motion control also inherently increases, as the MCA needs to correctly incorporate the kinematics of the additional motion subsystems.

The kinematic relations between the various simulator motion subsystems depend on where these subsystems are located (e.g., yaw-drive above or below the yaw-drive [15]), and affect the specific forces and rotational rates as presented in the simulator cabin. Although the kinematic relations for hexapods are known (e.g., [16]), to the best of our knowledge, a complete, formal derivation of the kinematics of driving simulators with additional motion systems has not been presented yet. Furthermore, there can be a difference in motion between the point where the simulator motion is applied (Motion Reference Point (MRP)) and where the driver is actually seated and perceives the motion (Cueing Reference Point (CRP)), which is often neglected to simplify the control problem. However, if simulators with additional subsystems are used, it is possible that these positional offsets cannot be neglected. If this offset is not accounted for through the correct kinematic relations, unwanted perceivable differences could occur between the MRP and the CRP. Thus, the role of the difference between MRP and CRP as a function of the simulator configuration must be investigated.

The contribution of this paper is threefold: First, the kinematic relations of the specific forces and rotational rates are derived for the MRP. This is done for three general simulator configurations: (i) a hexapod, (ii) a hexapod on an xy-drive and yaw-drive combination, and (iii) the same configuration as (ii), but with the yaw-drive *above* the hexapod. Using these results, the kinematic relations of many other motion simulators can be derived analogously. Second, the equations of motion relating the MRP and the CRP are derived. Third, by simulating these kinematic configurations using sinusoid forcing functions, the differences in inertial motion between the MRP and the CRP are quantified.

The structure of this paper is as follows. Section II describes the motion system kinematic relations. Section III describes the simulation results, followed by the discussion in Section IV, and the conclusion in Section V.

II. Kinematics of Motion Systems

A. Vehicle System

When driving in a simulator, ideally the motion of the simulator comes as close as possible to the real vehicle. The human perception of motion primarily occurs through the vestibular system [17], located near the inner ears, defining

[1] M. Kolff, J. Venrooij, and M. Schwienbacher are with the department of Research and Development at BMW Group, 80807 Munich, Germany, e-mail: Maurice.Kolff@bmw.de; Joost.Venrooij@bmw.de; Markus.Schwienbacher@bmw.de

[2] D. M. Pool, M. Mulder, and M. Kolff are with the section of Control & Simulation at Delft University of Technology, 2628HS Delft, The Netherlands, e-mail: d.m.pool@tudelft.nl; m.mulder@tudelft.nl; m.j.c.kolff@tudelft.nl

the Vehicle Reference Point (VRP), see Fig. 1. It are the specific forces and rotational rates occurring at this point in the real vehicle that the simulator should reproduce. When these motion data come from a real vehicle, an Inertial Measurement Unit (IMU) measures specific forces and rotational rates [18], which can be in an arbitrary position. The specific forces and rotational rates must be transformed from the position of the IMU to the VRP. The vector $\mathbf{r}_{IV}$ relates the IMU and VRP, see Fig. 1.

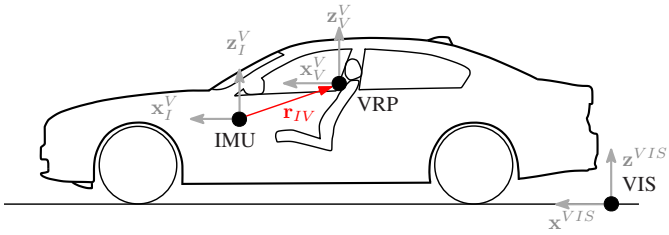

Fig. 1. The vehicle system, indicating the position of the Vehicle Reference Point (VRP) with respect to the Inertial Measurement Unit (IMU). The IMU measures the vehicle's specific forces and rotational rates. The vehicle's position and attitude are defined in the Vehicle Inertial System (VIS).

B. Simulator Systems

The aim of the MCA is to convert the vehicle model specific forces and rotational rates, as acting on the VRP, to generate platform accelerations and rotational rates acting on the human as close as possible to those experienced in a real vehicle. The specific forces and rotational rates are therefore required as inputs of the MCA and are generated by a vehicle model. Similar to the VRP in the real vehicle, for the simulator the CRP exists, in which the motion is perceived, e.g., see Fig. 2a. Thus, the motion applied in the MRP must aim at producing the proper motion in the CRP.

The three kinematic configurations studied in this paper are based on two systems present at BMW group. First, the Ruby Space (RS, Figure 2a) consists of a hexapod on top of a tripod. The latter acts as a combination of an xy-drive (by moving in x and y) and a yaw-drive (by rotating around z using the angle ψ_d), see [19], [20]. Second, the Sapphire Space (SS, Figure 2b), consisting of a large xy-drive at the bottom, a hexapod, and a yaw-drive. Both systems therefore have nine DoF to manipulate the three translations and three rotations of the vehicle mockup. The platform workspace limits are shown in Table I. Next to differences in size, the fundamental difference between the systems is where the additional yaw rotations ψ_d are applied. To calculate the resulting forces and rates acting on the vehicle mockup body frame B, as a function of the motion applied in the inertial system Simulator Inertial System (SIS), (conveniently located in the geometric center of the lowest simulator component), the contributions of the different DoFs must be combined. Because the hexapod of the Ruby Space is rotated through the tripod rotation, a local inertial system fixed to the tripod TIS is defined, see Figure 2a. In practice, the vector $\mathbf{r}_{MC}^B$ between MRP and CRP can also be different per simulator and vehicle mockup combination. To allow for a fair comparison between both systems, we assume $\mathbf{r}_{MC}^B = [x,\ y,\ z] = [-0.185,\ 0.40,\ 1.4]^\top$, which was measured in the Sapphire Space.

TABLE I

UNI-DIRECTIONAL WORKSPACE LIMITS OF THE TWO CONSIDERED MOTION SYSTEMS, RS = RUBY SPACE, SS = SAPPHIRE SPACE.

	hexapod						xy-drive		yaw-drive
	x_h	y_h	z_h	φ_h	θ_h	ψ_h	x_d	y_d	ψ_d
	m	m	m	deg	deg	deg	m	m	deg
RS	0.28	0.25	0.2	20	20	20	0.75	0.75	20
SS	1.4	1.2	0.8	25	25	35	9.57	7.85	180

C. Kinematic Chains

1) Six Degrees of Freedom: For a six DoF simulator, the attitude of the system with respect to the inertial reference system SIS is defined by the set of three Euler angles φ, θ, and ψ, describing the roll, pitch, and yaw angles, around the x, y, and z axes, respectively. In driving kinematics, the x-axis typically points forwards, y to the left (seen from the drivers perspective), and z upwards. The subsequent rotations over each angle are based intrinsically on the newly created coordinate system of the object by the previous rotation, such that the rotation sequence matters, see Fig. 3. The most common sequence is $z - y' - x''$ [21], i.e., the yaw rotation is applied first, followed by the pitch rotation, and then the roll rotation. The transformations due to these angles are calculated using the Euler transformation matrices, where the rotation angles are defined as counter-clockwise positive:

$$\mathbf{R}_x(\varphi) = \begin{bmatrix} 1 & 0 & 0 \\ 0 & \cos\varphi & -\sin\varphi \\ 0 & \sin\varphi & \cos\varphi \end{bmatrix},\ \mathbf{R}_y(\theta) = \begin{bmatrix} \cos\theta & 0 & \sin\theta \\ 0 & 1 & 0 \\ -\sin\theta & 0 & \cos\theta \end{bmatrix}, \tag{1}$$

$$\text{and } \mathbf{R}_z(\psi) = \begin{bmatrix} \cos\psi & -\sin\psi & 0 \\ \sin\psi & \cos\psi & 0 \\ 0 & 0 & 1 \end{bmatrix}. \tag{2}$$

A clockwise system would result in switched signs of the sin-terms. Commands to the motion system are generally defined in the inertial reference system SIS, or relative to its predecessor. To calculate the specific forces (including the gravity) on the cabin in its body-fixed system, one has to rotate the accelerations over the angles ψ, θ, and φ:

$$\begin{bmatrix} f_x \\ f_y \\ f_z \end{bmatrix}_M^B = (\mathbf{R}_x(\varphi)\mathbf{R}_y(\theta)\mathbf{R}_z(\psi))^\top \left(\begin{bmatrix} a_x \\ a_y \\ a_z \end{bmatrix}_{hex} + \begin{bmatrix} 0 \\ 0 \\ g \end{bmatrix} \right)^{SIS}. \tag{3}$$

Note that, in order to express the specific forces in terms of the motion in the inertial system, the *inverse* of the rotation sequence must be taken. This equals its transpose, because the rotational matrices are orthogonal (i.e., $\mathbf{R}^{-1} = \mathbf{R}^\top$). Because of the rotations, the specific forces in the body system of the simulator depend on the simulator orientation. This shows how sustained specific forces can be generated: rotations over the angles φ and θ induce sustained lateral or longitudinal specific force, respectively, due to the gravity component ("tilt-coordination", see [22]).

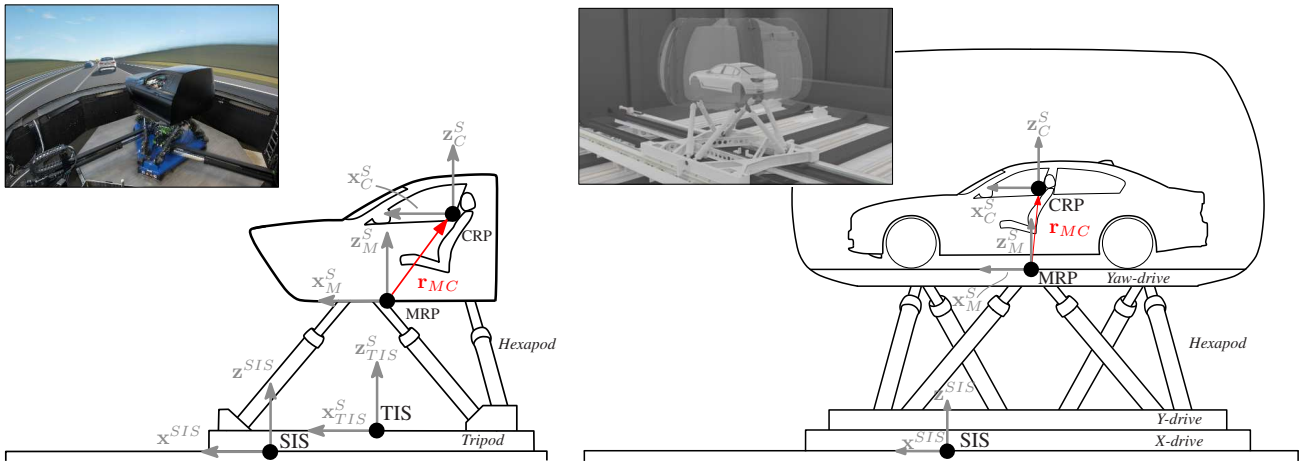

(a) The Ruby Space. Tripod actuators are not displayed.

(b) The Sapphire Space.

Fig. 2. Side views of the considered motion systems, showing the relevant reference points and coordinate systems.

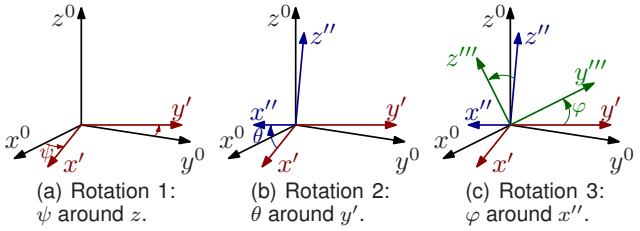

(a) Rotation 1: ψ around z.

(b) Rotation 2: θ around y'.

(c) Rotation 3: φ around x''.

Fig. 3. Three consecutive rotations using the order $z-y'-x''$ $(\psi-\theta-\psi)$.

For the rotational rates, a conversion from the Euler to body rates is necessary. Due to the importance of the rotation order, the body rates depend on any previously made rotation. The roll rate does not require a transformation, as it is the last rotation applied. The pitch rate is next in the sequence and must be transformed over the roll angle. Finally, the yaw rate must be transformed over the roll and pitch angles:

$$\begin{aligned}\begin{bmatrix}\omega_x\\ \omega_y\\ \omega_z\end{bmatrix}_M^B &= \begin{bmatrix}\dot\varphi\\ 0\\ 0\end{bmatrix} + \mathbf{R}_x^\top(\varphi)\begin{bmatrix}0\\ \dot\theta\\ 0\end{bmatrix} + \left(\mathbf{R}_x(\varphi)\mathbf{R}_y(\theta)\right)^\top\begin{bmatrix}0\\ 0\\ \dot\psi\end{bmatrix}\\ &= \begin{bmatrix}1 & 0 & -\cos\varphi\sin\theta\\ 0 & \cos\varphi & \sin\varphi\\ 0 & -\sin\varphi & \cos\varphi\cos\theta\end{bmatrix}\begin{bmatrix}\dot\varphi\\ \dot\theta\\ \dot\psi\end{bmatrix}.\end{aligned} \tag{4}$$

The resulting rotational rate vector $\boldsymbol{\omega}^B$ contains the rotational rates of the cabin, i.e., the *body rates* as a function of the *Euler rates*. (4) furthermore shows that only for small angles ($< 5°$) the matrix can be linearized to an identity matrix, such that the body rates approximately equal the Euler rates.

2) Nine Degrees of Freedom, yaw-drive below hexapod: Second, a configuration is investigated with an xy-drive and a yaw-drive at the below the hexapod. This configuration corresponds to the BMW's Ruby Space simulator, see Fig. 2a. As mentioned, it allows for additional translation in x_d and y_d, as well as additional rotation over an angle ψ_d. This latter, secondary rotation thus occurs below the hexapod. As the hexapod base moves with the tripod, the rotation sequence of the whole system is $\psi_d - \psi - \theta - \varphi$. As the two yaw contributions are consecutive, these contributions to the total yaw angle are additive, as they rotate around the same axis. The contribution of the hexapod accelerations do not rotate with the angle ψ_d, as they are defined in the local frame of the tripod TIS, on which the hexapod is located. Therefore, the total specific forces in the body frame become:

$$\begin{aligned}\begin{bmatrix}f_x\\ f_y\\ f_z\end{bmatrix}_M^B = \left(\mathbf{R}_x(\varphi)\,\mathbf{R}_y(\theta)\,\mathbf{R}_z(\psi)\right)^\top \Bigg(&\begin{bmatrix}a_x\\ a_y\\ a_z\end{bmatrix}_{hex}^{TIS} + \dots\\ &+ \mathbf{R}_z^\top(\psi_d)\left(\begin{bmatrix}a_x\\ a_y\\ 0\end{bmatrix}_{tri} + \begin{bmatrix}0\\ 0\\ g\end{bmatrix}\right)^{SIS}\Bigg).\end{aligned} \tag{5}$$

And similar to (4), the rotational rates are:

$$\begin{aligned}\begin{bmatrix}\omega_x\\ \omega_y\\ \omega_z\end{bmatrix}_M^B &= \begin{bmatrix}\dot\varphi\\ 0\\ 0\end{bmatrix} + \mathbf{R}_x^\top(\varphi)\begin{bmatrix}0\\ \dot\theta\\ 0\end{bmatrix} + \left(\mathbf{R}_x(\varphi)\mathbf{R}_y(\theta)\right)^\top\begin{bmatrix}0\\ 0\\ \dot\psi + \dot\psi_d\end{bmatrix}\\ &= \begin{bmatrix}1 & 0 & -\cos\varphi\sin\theta\\ 0 & \cos\varphi & \sin\varphi\\ 0 & -\sin\varphi & \cos\varphi\cos\theta\end{bmatrix}\begin{bmatrix}\dot\varphi\\ \dot\theta\\ \dot\psi + \dot\psi_d\end{bmatrix}.\end{aligned} \tag{6}$$

The resulting rotational rate vector $\boldsymbol{\omega}$ contains the rotational rates of the cabin. Note that the presence of a yaw-drive at the bottom thus does not affect the effect of the linearization, i.e., it is identical to (4). Thus, for small angles φ and θ, the body rates might still approximate the Euler rates.

3) Nine Degrees of Freedom, yaw-drive above hexapod: Finally, the kinematic chain is considered for the same system, but with the yaw-drive above the hexapod (corresponding to BMW's Sapphire Space, see Fig. 2b). Again, its rotation sequence is fixed, although the yaw-drive rotation is here always the *last* in the chain, i.e., the order is $\psi-\theta-\varphi-\psi_d$. A benefit of this is that the yaw-drive rotation can be fully used to generate yaw motion, as it is unaffected by the rotations of the other DoF. This is opposed to the case with the yaw-drive below, where the yaw motion is always

entangled with the roll and pitch motion. An important drawback, however, is that the yaw rotation contributions of the yaw-drive and the hexapod are *not* additive anymore, as these do not rotate around the same axis if φ and θ are non-zero. Therefore, an additional rotation matrix $\mathbf{R}_z(\psi_d)$ is required, such that the specific forces become:

$$\begin{bmatrix} f_x \\ f_y \\ f_z \end{bmatrix}_M^B = \left(\mathbf{R}_z(\psi_d)\,\mathbf{R}_x(\varphi)\,\mathbf{R}_y(\theta)\,\mathbf{R}_z(\psi)\right)^\top \ldots \\ \ldots \left(\begin{bmatrix} a_x \\ a_y \\ 0 \end{bmatrix}_{xy} + \begin{bmatrix} a_x \\ a_y \\ a_z \end{bmatrix}_{hex} + \begin{bmatrix} 0 \\ 0 \\ g \end{bmatrix} \right)^{SIS}. \quad (7)$$

Furthermore, the rotational rates become:

$$\begin{aligned} \begin{bmatrix} \omega_x \\ \omega_y \\ \omega_z \end{bmatrix}_M^B &= \begin{bmatrix} 0 \\ 0 \\ \dot{\psi}_d \end{bmatrix} + \mathbf{R}_z^\top(\psi_d) \begin{bmatrix} \dot{\varphi} \\ 0 \\ 0 \end{bmatrix} + \left(\mathbf{R}_z(\psi_d)\mathbf{R}_x(\varphi)\right)^\top \begin{bmatrix} 0 \\ \dot{\theta} \\ 0 \end{bmatrix} \\ &\quad + \left(\mathbf{R}_z(\psi_d)\mathbf{R}_x(\varphi)\mathbf{R}_y(\theta)\right)^\top \begin{bmatrix} 0 \\ 0 \\ \dot{\psi} \end{bmatrix} \quad (8) \\ &= \begin{bmatrix} 0 & c_{\psi_d} & s_{\psi_d} & -c_\varphi s_\theta \\ 0 & -s_{\psi_d} & c_{\psi_d} c_\varphi & s_\varphi \\ 1 & 0 & -c_{\psi_d} s_\varphi & c_\varphi c_\theta \end{bmatrix} \begin{bmatrix} \dot{\psi}_d \\ \dot{\varphi} \\ \dot{\theta} \\ \dot{\psi} \end{bmatrix}, \end{aligned}$$

where $s_\star$ and $c_\star$ are $\sin(\star)$ and $\cos(\star)$, respectively.

This shows a key difference compared to (4) and (6), because here the transformation matrix includes terms of the yaw-drive as well. Due to the larger allowable rotations of this device, the small angle approximation is not valid anymore. Therefore, it cannot be assumed that the body rates equal the Euler rates. This complicates the motion control, as it must include the non-linear conversion matrix of (8).

D. Reference point shift

The previously derived specific force and rotational rate definitions apply in the MRP. As the motion of the simulator is to be calculated in the CRP, the positional offset $\mathbf{r}_{MC}^B$ between these two points should be accounted for. When assuming the simulator is a rigid body, the body rates do not depend on location of the reference point ($\boldsymbol{\omega}^B = \boldsymbol{\omega}_M^B = \boldsymbol{\omega}_C^B$) [21]. The specific forces require a transformation, however. As vector $\mathbf{r}_{MC}^B$ points from the MRP to the CRP:

$$\mathbf{r}_C^I = \mathbf{r}_M^I + \mathbf{r}_{MC}^I = \mathbf{r}_M^I + \mathbf{T}_{IB}\mathbf{r}_{MC}^B, \quad (9)$$

with I short for the inertial SIS frame and B for the body-fixed frame. When taking its time derivative to obtain the velocity:

$$\begin{aligned} \mathbf{v}_C^I &= \frac{\mathrm{d}\mathbf{r}_C^I}{\mathrm{d}t} = \frac{\mathrm{d}\mathbf{r}_M^I}{\mathrm{d}t} + \frac{\mathrm{d}(\mathbf{T}_{IB}\mathbf{r}_{MC}^B)}{\mathrm{d}t} \\ &= \dot{\mathbf{r}}_M^I + \dot{\mathbf{T}}_{IB}\mathbf{r}_{MC}^B + \mathbf{T}_{IB}\dot{\mathbf{r}}_{MC}^B, \end{aligned} \quad (10)$$

Note, that $\mathbf{T}_{BI} = \left(\mathbf{R}_x(\varphi)\mathbf{R}_y(\theta)\mathbf{R}_z(\psi)\right)^\top$ for a hexapod, $\mathbf{T}_{BI} = \left(\mathbf{R}_x(\varphi)\mathbf{R}_y(\theta)\mathbf{R}_z(\psi+\psi_d)\right)^\top$ for Ruby Space, and $\mathbf{T}_{BI} = \left(\mathbf{R}_z(\psi_d)\mathbf{R}_x(\varphi)\mathbf{R}_y(\theta)\mathbf{R}_z(\psi)\right)^\top$ for Sapphire Space, as derived earlier. Taking the time derivative again to obtain the acceleration and transforming to the body system:

$$\begin{aligned} \mathbf{a}_C^B &= \mathbf{T}_{BI}\left(\frac{\mathrm{d}\mathbf{v}_M^I}{\mathrm{d}t} + \frac{\mathrm{d}(\dot{\mathbf{T}}_{IB}\mathbf{r}_{MC}^B)}{\mathrm{d}t} + \frac{\mathrm{d}(\mathbf{T}_{BI}\dot{\mathbf{r}}_{MC}^B)}{\mathrm{d}t} + \mathbf{T}_{IB}\ddot{\mathbf{r}}_{MC}^B\right) \\ &= \mathbf{T}_{BI}\left(\mathbf{a}_M^I + \ddot{\mathbf{T}}_{IB}\mathbf{r}_{MC}^B + \dot{\mathbf{T}}_{IB}\dot{\mathbf{r}}_{MC}^B + \dot{\mathbf{T}}_{IB}\dot{\mathbf{r}}_{MC}^B + \mathbf{T}_{IB}\ddot{\mathbf{r}}_{MC}^B\right) \\ &= \mathbf{a}_M^B + \mathbf{T}_{BI}\ddot{\mathbf{T}}_{IB}\mathbf{r}_{MC}^B + 2\mathbf{T}_{BI}\dot{\mathbf{T}}_{IB}\dot{\mathbf{r}}_{MC}^B + \mathbf{a}_{MC}^B. \end{aligned} \quad (11)$$

The derivative of the transformation matrix $\mathbf{T}_{IB}$ can be expressed through a tensor matrix [23], [21], [24]:

$$\mathbf{S}(\boldsymbol{\omega}) = \dot{\mathbf{T}}_{IB}\mathbf{T}_{IB}^\top \rightarrow \dot{\mathbf{T}}_{IB} = \frac{\mathbf{S}(\boldsymbol{\omega})}{\mathbf{T}_{IB}^\top} = \mathbf{S}(\boldsymbol{\omega})\mathbf{T}_{IB} \quad (12)$$

with:

$$\mathbf{S}(\boldsymbol{\omega}) = \mathbf{S}(\omega_x) + \mathbf{S}(\omega_y) + \mathbf{S}(\omega_z) = \begin{bmatrix} 0 & -\omega_z & \omega_y \\ \omega_z & 0 & -\omega_x \\ -\omega_y & \omega_x & 0 \end{bmatrix}. \quad (13)$$

The derivative of $\dot{\mathbf{T}}_{IB}$ can be found using the chain rule:

$$\begin{aligned} \ddot{\mathbf{T}}_{IB} = \frac{\mathrm{d}(\mathbf{S}(\boldsymbol{\omega})\mathbf{T}_{IB})}{\mathrm{d}t} &= \dot{\mathbf{S}}(\boldsymbol{\omega})\mathbf{T}_{IB} + \mathbf{S}(\boldsymbol{\omega})\dot{\mathbf{T}}_{IB} \\ &= \dot{\mathbf{S}}(\boldsymbol{\omega})\mathbf{T}_{IB} + \mathbf{S}^2(\boldsymbol{\omega})\mathbf{T}_{IB}. \end{aligned} \quad (14)$$

Subsequently, (12) and (14) can be substituted into (11):

$$\mathbf{a}_C^B = \mathbf{a}_M^B + \dot{\mathbf{S}}(\boldsymbol{\omega})\mathbf{r}_{MC}^B + \mathbf{S}^2(\boldsymbol{\omega})\mathbf{r}_{MC}^B + 2\mathbf{S}(\boldsymbol{\omega})\dot{\mathbf{r}}_{MC}^B + \mathbf{a}_{MC}^B, \quad (15)$$

where $\dot{\mathbf{S}}(\boldsymbol{\omega}_C)$ contains the time derivatives of the elements in $\mathbf{S}(\boldsymbol{\omega}_C)$, i.e., the rotational accelerations. This expresses the total acceleration in the CRP, which is converted to the total specific force in the CRP by substituting $\mathbf{a}_M^B$ with $\mathbf{f}_M^B$:

$$\mathbf{f}_C^B = \underbrace{\mathbf{f}_M^B}_{\text{(i)}} + \underbrace{\dot{\mathbf{S}}(\boldsymbol{\omega})\mathbf{r}_{MC}^B}_{\text{(ii)}} + \underbrace{\mathbf{S}^2(\boldsymbol{\omega})\mathbf{r}_{MC}^B}_{\text{(iii)}} + \underbrace{2\mathbf{S}(\boldsymbol{\omega})\dot{\mathbf{r}}_{MC}^B}_{\text{(iv)}} + \underbrace{\mathbf{a}_{MC}^B}_{\text{(v)}}. \quad (16)$$

This is the main kinematic relation for rigid bodies. It consists of (i) the acceleration of the MRP in the body system, (ii) the tangential acceleration, (iii) the centripetal acceleration, (iv) the Coriolis acceleration, and (v) the relative acceleration between the CRP and MRP [25]. The relation itself does not depend on the kinematic configuration of the motion system. However, the centripetal, tangential, and Coriolis acceleration depend on the rotational rates $\boldsymbol{\omega}_C^B$ of the rigid body, corresponding to (4), (6), or (8), and are thus implicitly configuration-specific. The element $\mathbf{f}_M^B$ contain the specific forces in the MRP in the body frame, which corresponds to (3), (5), or (7).

III. Simulations

A. Testing Procedure

A testing procedure was used to compare the specific forces between the MRP and the CRP, based on (16):

$$\begin{aligned} \Delta\mathbf{f}_{CM}^B &= \mathbf{f}_C^B - \mathbf{f}_M^B \\ &= \dot{\mathbf{S}}(\omega)\mathbf{r}_{MC}^B + \mathbf{S}^2(\omega)\mathbf{r}_{MC}^B + 2\mathbf{S}(\omega)\dot{\mathbf{r}}_{MC}^B + \mathbf{a}_{MC}^B. \end{aligned} \quad (17)$$

The following motion configurations are tested, based on the three system introduced in Section II-B:

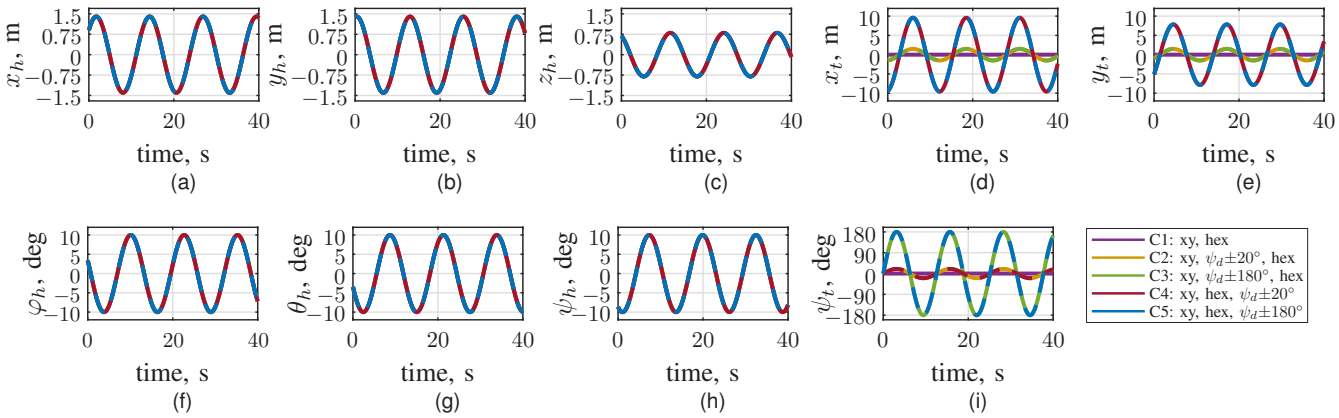

Fig. 4. Forcing functions of the nine Degree of Freedom (DoF)s, simulated for $\omega = 0.5$ rad/s.

C1: An xy-drive and a hexapod.
C2: An xy-drive, a yaw-drive ($\psi_d = \pm 20°$), and a hexapod.
C3: An xy-drive, a yaw-drive ($\psi_d = \pm 180°$), and a hexapod.
C4: An xy-drive, a hexapod, and a yaw-drive ($\psi_d = \pm 20°$).
C5: An xy-drive, a hexapod, and a yaw-drive ($\psi_d = \pm 180°$).

Comparing conditions C1, C2, and C4 allows for investigating the role of the presence and location of the yaw-drive for an excitation angle similar to that of Ruby Space. C3 and C5 show the extent to which additional yaw-drive excitation affects the difference between MRP and CRP.

Note that the size of the xy-drive and the translational channels of the hexapod are in fact irrelevant: as we look at the difference between MRP and CRP, both scale up equivalently in terms of acceleration if the size of the xy-drive changes. Thus, this has no effect on any further analyses on differences between the points.

A sinusoidal input was applied to the position signal of the various DoF of the considered motion configurations of the shape:

$$p(t) = A \sin(\tilde{\omega} t + \phi), \tag{18}$$

with its derivative as the velocity signal:

$$v(t) = \tilde{\omega} A \cos(\tilde{\omega} t + \phi), \tag{19}$$

and the double derivative as the acceleration signal:

$$a(t) = -\tilde{\omega}^2 A \sin(\tilde{\omega} t + \phi), \tag{20}$$

with the frequency $\tilde{\omega}$ in rad/s, and the phase ϕ in rad. The amplitudes A were chosen to fit the workspace of the simulator in each DoF, i.e., the positional workspace limits of Table I. The amplitudes of the rotational channels were set smaller ($\pm 10°$, a typical angle used for tilt-coordination [22]) than the rotational limits of the motion systems (See Table I), as hexapods cannot fully rotate in all three rotational DoFs at the same time [25] due to their coupled DoFs. To represent representative motion of a vehicle, such as a 90° corner taken in a 3 s time span [20], the frequency was set at $\tilde{\omega} = \frac{\pi \cdot 90°}{180 \cdot 3} = 0.5$ rad/s in all motion channels.

To avoid situations where contributions of the sinusoids may (partially) cancel each other out, the phases were set different in each DoF: $\phi = 2\pi \cdot [\frac{1}{9}, \frac{2}{9}, \frac{3}{9}, \frac{4}{9}, \frac{5}{9}, \frac{6}{9}, \frac{7}{9}, \frac{8}{9}, \frac{9}{9}]$ for $[x_h,\ y_h,\ z_h,\ \phi_h,\ \theta_h,\ \psi_h,\ x_d,\ y_d,\ \psi_d]$. The resulting sinusoids were simulated for 40 s, as shown in Figs. 4a-4i.

B. Results

Figs. 5a-5c show the difference in simulated specific forces for f_x, f_y, and f_z, respectively, between the MRP and the CRP. The rotational rates ω are not shown, as for a rigid body these are unaffected by a reference point shift, see Section II-D, and thus the difference between the MRP and the CRP is zero. The positive and negative perceptual threshold are plotted as dashed lines, corresponding to values of ± 0.05 m/s^2 [26]. Differences above these thresholds can be expected to lead to perceivable differences between the MRP and the CRP. For conditions C1, C2, and C4, differences between the reference points are present, but only sometimes marginally exceed the perceptual threshold. For conditions C3 and C5, corresponding to the large yaw-drive excursions of $\pm 180°$, the difference becomes noticeable and reaches its largest difference in f_y (-1.5 m/s^2). Some care should be taken with the interpretation, as a higher amplitude of the sinusoidal forcing functions between the conditions also implies that the Euler angle derivatives are different between the conditions. This subsequently results in higher rotational rates. The forcing functions applied to the different motion systems are therefore not the same. However, this shows a inherent property of larger yaw-drives, as these allow for, and practically will have larger rotational rates.

To generalize the results of the yaw-drive excitation, the results are generated for the complete range of yaw-drive amplitude A_{ψ_d}, corresponding to the maximum excitation of the yaw-drive, between 0° and ±180°. To quantify the overall difference between the MRP and the CRP specific force signals in x, y, and z direction, the norm [27] is used:

$$\Delta f_n(t) = \sqrt{(\Delta f^B_{xCM})^2 + (\Delta f^B_{yCM})^2 + (\Delta f^B_{zCM})^2}. \tag{21}$$

For each yaw-drive angle, the maximum absolute values of the norm values ($\max[|\Delta f_n(t)|]$) are calculated, i.e., the

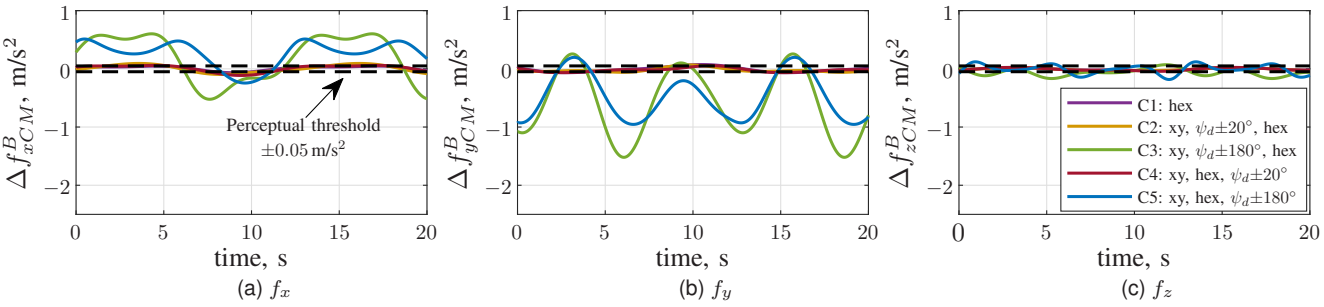

Fig. 5. The difference between the specific forces simulated in the MRP ($\mathbf{r} = [0,\ 0,\ 0]^T$) and the CRP ($\mathbf{r} = [-0.185,\ 0.40,\ 1.4]^T$), for the five considered motion system configurations with $\omega = 0.5$ rad/s. The colors correspond to the conditions defined in Fig. 4, the black dashed lines are the perceptual threshold of $\pm 0.05\,\mathrm{m/s^2}$ from [26].

largest occurring mismatch, see Fig. 6. These are plotted as function of the yaw-drive amplitude A_{ψ_d} for the configurations with the yaw-drive below (grey) and above (black). The perceptual threshold is again plotted as a dashed line, of which also the norm of the three directions is calculated, such that the line corresponds to $0.087\,\mathrm{m/s^2}$. The figure shows

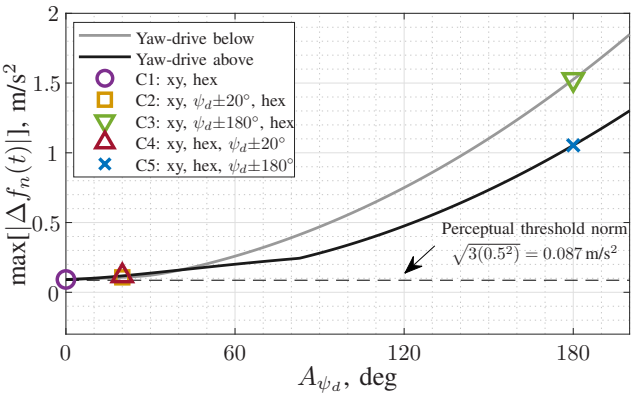

Fig. 6. Maximum norm of the difference in specific force between the Motion Reference Point (MRP) and the Cueing Reference Point (CRP), as a function of yaw-drive forcing function amplitude.

that for C1 (without a yaw-drive), the difference between the MRP and the CRP can already be noticed, as it lies above the perceptual threshold at $0.09\,\mathrm{m/s^2}$. When a yaw-drive is added and excites to $\pm 20°$, corresponding to the conditions C2 and C4, the differences are still limited at $0.11\,\mathrm{m/s^2}$ and $0.12\,\mathrm{m/s^2}$. At larger yaw-drive angles, the norm difference increases more than linearly. At the conditions C3 and C5, with a $\pm 180°$ yaw-drive, the norm differences are $1.05\,\mathrm{m/s^2}$ and $1.53\,\mathrm{m/s^2}$. This will lead to erroneous accelerations perceived in the simulator.

IV. Discussion

The simulation results show that the configurations with the large excitation yaw-drive ($\pm 180°$), i.e., C3 and C5, lead to large differences in the specific forces between the MRP and CRP. For simulators with extended yaw-drive capabilities, these results emphasize the crucial importance of utilizing the correct reference point in an MCA. Incorrect reference point selection will directly lead to significant spurious specific forces, which can affect driving simulator experiments and increase the occurrence of simulator sickness. For smaller yaw-drive angles ($\pm 20°$, C2 and C4) or no yaw-drive at all (C1) the differences are smaller ($0.11\,\mathrm{m/s^2}$, $0.12\,\mathrm{m/s^2}$, and $0.09\,\mathrm{m/s^2}$, respectively), but still slightly above the perception threshold ($0.087\,\mathrm{m/s^2}$). This shows that even for such smaller systems, the difference cannot be ignored in the current simulator configurations.

Although condition C5, with the $\pm 180°$ yaw-drive above leads to smaller differences than C3, *both* show large deviations between the MRP and the CRP. A yaw-drive at the bottom shows an another, important benefit: for small roll and pitch angles ($5 - 10°$ [21]) of the hexapod, see (6), the system can be linearized. This reduces the complexity compared to the yaw-drive on top, as here the additional contribution of the yaw-drive (see (8)) implies that the same linearization procedure cannot be made. This could be of great impact on Model-Predictive Control (MPC) MCAs [28], as the linearization can lead to a simplified MCA. For example, in an MPC MCA, the non-linear structure of (16) could be avoided, resulting in an easier control problem. A benefit of a yaw-drive at the top is that its contribution to the yaw rate does not require a transformation between ψ_d and ω_z. Which configuration is superior might thus depend on the properties of the MCA under consideration.

As a note on limitations, we stress that the presented results on the deviations between the MRP and the CRP are a function of several variables. First, note that the perceptual thresholds used in this paper by [26] were measured unidirectionally, which are likely higher when measured under motion in all directions. In practice the deviation for the smaller systems (C1, C2 and C4) might therefore be of no practical meaning. The specific forces are also directly a function of the distance between the MRP and the CRP ($\mathbf{r}^B_{MC}$), see (16). Most simulator systems and mock-up combinations at BMW (See [12]) are similar in this regard, such that the values of $\mathbf{r}^B_{MC}$ in this paper are representative. If a simulator is considered that is smaller than the one presented in this paper, the degree of erroneous specific forces also decreases. Therefore, we recommend the results and interpretations presented in this paper to be used as guidelines, rather than a one-fits-all answer.

V. Conclusion

This paper presented the derivation of the kinematic relations (specific forces and rotational rates) of three types of driving simulators as currently in use at BMW: a hexapod, a hexapod and an xy-drive with a yaw-drive below, and the same system, but with the yaw-drive on top. The results show that increasing the excitation of a yaw-drive increases the difference between the Motion Reference Point (MRP) (the point where the motion is applied) and the Cueing Reference Point (CRP) (where the driver perceives the motion). For a hexapod, with or without a $\pm 20^\circ$ yaw-drive, this difference is close to the perceptual threshold, such that the motion control of the simulator might be simplified by not correcting for the difference between MRP and CRP. For systems with a $\pm 180^\circ$ yaw-drive, such large differences between the motion in the MRP and the CRP are present, that erroneous specific forces in the order of $1\,\mathrm{m/s^2}$ are present. Here, the motion control should account for the difference in MRP and CRP, complicating the motion control. This finding is irrespective of whether the yaw-drive on top or below the hexapod, although the difference between MRP and CRP are larger when the yaw-drive is below the hexapod. However, when the yaw-drive is on top, the resulting non-linear relations to calculate the body rates greatly increase kinematic complexity, which is a crucial factor for state-of-the-art MPC-based MCAs. With increasing kinematic complexity of state-of-the-art driving simulators, this increased understanding of the kinematic relations and the effects of the MCA reference point position is crucial knowledge for engineers and scientists testing and developing intelligent vehicles.

References

[1] J. Lindner, A. Keler, G. Grigoropoulos, P. Malcolm, F. Denk, P. Brunner, and K. Bogenberger, "A coupled driving simulator to investigate the interaction between bicycles and automated vehicles," in *25th IEEE International Conference on Intelligent Transportation Systems (ITSC)*, 2022, pp. 1335–1341.

[2] C. Chai, X. Zeng, I. Alvarez, and M. S. Elli, "Evaluation of responsibility-sensitive safety (rss) model based on human-in-the-loop driving simulation," in *23rd IEEE International Conference on Intelligent Transportation Systems (ITSC)*, 2020, pp. 1–7.

[3] P. Bazilinskyy, L. Kooijman, D. Dodou, and J. C. de Winter, "Coupled simulator for research on the interaction between pedestrians and (automated) vehicles," in *Driving Simulation Conference Europe. Antibes, France*, 2020.

[4] K. Stahl, G. Abdulsamad, K.-D. Leimbach, and Y. A. Vershinin, "State of the art and simulation of motion cueing algorithms for a six degree of freedom driving simulator," in *17th IEEE International Conference on Intelligent Transportation Systems (ITSC)*, 2014, pp. 537–541.

[5] S. Casas-Yrurzum, C. Portalés-Ricart, P. Morillo-Tena, and C. Cruz-Neira, "On the objective evaluation of motion cueing in vehicle simulations," *IEEE Transactions on Intelligent Transportation Systems*, vol. 99, pp. 1–13, 2020.

[6] C. Himmels, J. Venrooij, M. Gmünder, and A. Riener, "The influence of simulator and driving scenario on simulator sickness," in *Proceedings of the Driving Simulation Conference 2022 Europe*, Strasbourg, France, 2022, pp. 29–36.

[7] R. Romano, G. Markkula, E. Boer, H. Jamson, A. Bean, A. Tomlinson, A. Horrobin, and E. Sadraei, "An objective assessment of the utility of a driving simulator for low mu testing," *Transportation Research Part F: Traffic Psychology and Behaviour*, vol. 65, no. 1, pp. 34–45, 2019.

[8] M. Ghafarian, M. Watson, N. Mohajer, D. Nahavandi, P. Kebria, and S. Mohamed, "A review of dynamic vehicular motion simulators: Systems and algorithms," *IEEE Access*, vol. 11, pp. 36 331–36 348, 2023.

[9] D. Stewart, "A Platform with Six Degrees of Freedom," *Proceedings of the Institution of Mechanical Engineers*, vol. 180, no. 1, pp. 371–386, 1965.

[10] V. E. Gough, "Universal tyre test machine," in *Proceedings of the FISITA 9th International Technical Congress*, London, United Kingdom, 1962, pp. 117–137.

[11] G. Baumann, W. Krantz, and J. Pitz, "Evaluation of steering feel and vehicle handling in the stuttgart driving simulator (bewertung von lenkgefühl und fahrverhalten im stuttgarter fahrsimulator)," in *Proceedings of the 5th International Munich Chassis Symposium 2014*, 2014, pp. 201–215.

[12] M. Kolff, J. Venrooij, M. Schwienbacher, D. M. Pool, and M. Mulder, "Motion cueing quality comparison of driving simulators using oracle motion cueing," in *Proceedings of the Driving Simulation Conference 2022 Europe*, Strasbourg, France, 2022, p. 111–118.

[13] Y. S. Chiew, M. K. Abdul Jalil, and M. Hussein, "Kinematic modeling of driving simulator motion platform," in *Proceedings of the 2008 IEEE Conference on Innovative Technologies in Intelligent Systems and Industrial Applications*, Cyberjaya, Malaysia, 2008, pp. 30–34.

[14] Z. Fang, D. Wautier, and A. Kemeny, "Fft based optimal mca for ad/adas driving tests," in *Proceedings of the Driving Simulation Conference 2022 Europe*, Strasbourg, France, 2022, p. 119–126.

[15] Z. Fang, M. Tsushima, E. Kitahara, N. Machida, D. Wautier, and A. Kemeny, "Motion cueing algorithm for high performance driving simulator using yaw table," *IFAC-PapersOnLine*, vol. 50, no. 1, pp. 15 965–15 970, 2017.

[16] M. Bruschetta, C. Cenedese, A. Beghi, and F. Maran, "A motion cueing algorithm with look-ahead and driver characterization: Application to vertical car dynamics," *IEEE Transactions on Human-Machine Systems*, vol. 48, no. 1, pp. 6–16, 2018.

[17] J. Houck, R. Telban, and F. Cardullo, "Motion cueing algorithm development: Human-centered linear and nonlinear approaches," State University of New York, Tech. Rep. CR-2005-213747, 2005.

[18] D. W. P. Nogueira, R. M. Bacurau, D. A. Lima, F. O. Silva, and A. M. Neto, "In motion low-cost imu-to-vehicle alignment for intelligent vehicle applications using kalman filter," in *24th IEEE International Conference on Intelligent Transportation Systems (ITSC)*, 2021, pp. 92–97.

[19] M. Kolff, J. Venrooij, M. Schwienbacher, D. M. Pool, and M. Mulder, "Quality comparison of motion cueing algorithms for urban driving simulations," in *Proceedings of the Driving Simulation Conference 2021 Europe*, Munich, Germany, 2021, p. 141–148.

[20] M. Kolff, J. Venrooij, M. Schwienbacher, D.M. Pool, and M. Mulder, "Reliability and models of subjective motion incongruence ratings in urban driving simulations," *IEEE Transactions on Human-Machine Systems*, 2023, under review.

[21] J. Diebel, "Representing attitude: Euler angles, unit quaternions, and rotation vectors," 2006.

[22] A. Stratulat, V. Roussarie, J. Vercher, and C. Bourdin, "Does tilt/translation ratio affect perception of deceleration in driving simulators?" *Journal of vestibular research: equilibrium & Orientation*, vol. 21, no. 3, pp. 127–139, 2011.

[23] M. Olivari, P. Pretto, J. Venrooij, and H. Bülthoff, "Defining the kinematic requirements for a theoretical driving simulator," *Transportation Research Part F: Traffic Psychology and Behaviour*, vol. 61, pp. 5–15, 2019.

[24] T. Buschmann, "Dynamics and control of redundant robots," Habilitation Thesis, Technische Universität München, 2014.

[25] F. Ellensohn, "Urban Motion Cueing Algorithms - Trajectory Optimization for Driving Simulators," PhD Dissertation, Technische Universität München, 2020.

[26] G. Reymond and A. Kemeny, "Motion cueing in the renault driving simulator," *Vehicle System Dynamics*, vol. 34, no. 4, pp. 249–259, 2000.

[27] N. A. Pouliot, C. M. Gosselin, and M. A. Nahon, "Motion Simulation Capabilities of Three-Degree-of-Freedom Flight Simulators," *Journal of Aircraft*, vol. 35, no. 1, pp. 9–17, 1998.

[28] A. Lamprecht, D. Steffen, K. Nagel, J. Haecker, and K. Graichen, "Online model predictive motion cueing with real-time driver prediction," *IEEE Transactions on Intelligent Transportation Systems*, pp. 1–15, 2021.